Physics in Medicine & Biology

ACCEPTED MANUSCRIPT

Magnetic resonance electrical property mapping at 21.1 T: a study of conductivity and permittivity in phantoms, <i>ex vivo</i> tissue and <i>in vivo</i> ischemia

Title

Magnetic Resonance Electrical Property Mapping at 21.1 T: A study of conductivity and permittivity in phantoms, *ex vivo* tissue and *in vivo* ischemia

Running Title: EPT at 21.1 T

Authors

Ghoncheh Amouzandeh[a,b], Frederic Mentink-Vigier[b], Shannon Helsper[b,c], F. Andrew Bagdasarian[b,c], Jens T. Rosenberg[b] and Samuel C. Grant[b,c]

[a] Department of Physics, Florida State University, Tallahassee, FL, USA

[b] The National High Magnetic Field Laboratory, Florida State University, Tallahassee, FL, USA.

[c] Department of Chemical & Biomedical Engineering, FAMU-FSU College of Engineering, Tallahassee, FL, USA

Corresponding Author

Samuel C. Grant, PhD

National High Magnetic Field Laboratory, Center for Interdisciplinary Magnetic Resonance

1800 E. Paul Dirac Drive, Tallahassee, FL 32310

Email: grant@magnet.fsu.edu

Phone: 01-850-645-7197

Fax: 01-850-644-1366

Keywords: MRI; magnetic resonance electrical properties tomography; electrical conductivity; electrical permittivity; B_1 inhomogeneity; 21.1 Tesla; transient cerebral ischemia

Acknowledgements

This work was performed at the National High Magnetic Field Laboratory, which is supported by National Science Foundation Cooperative Agreement (DMR-1157490, DMR-1644779) and the State of Florida. Funding support was provided by the NHMFL User Collaboration Grants Program as well as the National Institute of Health (R01-NS102395). The authors would like to thank Dr. C.A.T van der Berg for helpful discussions and also Nastaren Abad and Arash Yunesi for their insights and help in reviewing this manuscript.

Abstract

Objective: Electrical properties (EP), namely conductivity and permittivity, can provide endogenous contrast for tissue characterization. Using electrical property tomography (EPT), maps of EP can be generated from conventional MRI data. This report investigates the feasibility and accuracy of EPT at 21.1 T for multiple RF coils and modes of operation using phantoms. Additionally, it demonstrates the EP of the *in vivo* rat brain with and without ischemia.

Methods: Helmholtz-based EPT was implemented in its Full-form, which demands the complex B_1^+ field, and a simplified form requiring either just the B_1^+ field phase for conductivity or the B_1^+ field magnitude for permittivity. Experiments were conducted at 21.1 T using birdcage and saddle coils operated in linear or quadrature transceive mode, respectively. EPT approaches were evaluated using a phantom, *ex* and *in vivo* Sprague-Dawley rats under naïve conditions and ischemic stroke via transient middle cerebral artery occlusion.

Results: Different conductivity reconstruction approaches applied to the phantom displayed average errors of 12-73% to the target acquired from dielectric probe measurements. Permittivity reconstructions showed higher agreement and an average 3-8% error to the target depending on reconstruction approach. Conductivity and permittivity of *ex* and *in vivo* rodent brain were measured. Elevated EP in the ischemia region correlated with the increased sodium content and the influx of water intracellularly following ischemia in the lesion were detected.

Discussion: The Full-form technique generated from the linear birdcage provided the best accuracy for EP of the phantom. Phase-based conductivity and magnitude-based permittivity mapping provided reasonable estimates but also demonstrated the limitations of Helmholtz-based EPT at 21.1 T. Permittivity reconstruction was improved significantly over lower fields, suggesting a novel metric for *in vivo* brain studies. EPT applied to ischemic rat brain proved sensitivity to physiological changes, motivating the future application of more advanced reconstruction approaches.

Total Word Count (abstract): 296

Manuscript Word Count: 7285

Introduction

Electrical properties (EP), *i.e.* conductivity and permittivity, are fundamental properties of biological tissue that may vary under physiological and pathological conditions (Schepps and Foster 1980, Joines *et al* 1994, Lazebnik *et al* 2007, Hancu *et al* 2015). Therefore, EP of biological tissue potentially could be used as an endogenous quantitative contrast to provide additional information to MRI for diagnostic and therapeutic monitoring purposes (Liu *et al* 2017b, Katscher and van den Berg 2017, Xiaotong Zhang *et al* 2014). EP are functions of the frequency of the applied radiofrequency (RF) field and vary relative to tissue biophysical properties, such as water content, ionic concentrations and compartmentalization (*e.g.*, intra- versus extracellular spaces) (Ouwerkerk *et al* 2007, Pethig 1984, Schwan and Foster 1989, Gabriel *et al* 1996). Knowledge of EP is also valuable for accurate safety assessments requiring *in vivo* specific absorption rate (SAR) mapping in high-field MRI (Voigt *et al* 2012, Zhang *et al* 2014, Collins *et al* 2004, Zhang *et al* 2013b). In recent years, a group of techniques, commonly referred to as MR electrical property tomography (MREPT or EPT), have been proposed to image tissue EP noninvasively at Larmor frequency with minimal alteration of existing MR scanner instrumentation or RF architecture (Katscher *et al* 2009, Xiaotong Zhang *et al* 2010, Katscher *et al* 2013b, Liu *et al* 2013). Although these approaches have been conducted more commonly at clinical field strengths, the challenges and benefits of applying standard EPT techniques at ultra-high preclinical fields (those above 9.4 T) have not been studied previously. EPT could be affected dramatically at higher frequencies because of constraints placed on certain approximations used in EPT reconstruction as well as RF penetration and skin depth. The current report demonstrates the possibility of implementing EPT at 21.1 T, the highest preclinical field available, for phantoms, *ex vivo* tissue and *in vivo* rodent brain. At this field strength, notable accuracy in permittivity reconstructions has been achieved that provided insight into the relative permittivity differences in the ischemic brain lesion.

Determining EP from the MRI radio frequency (RF) field was first proposed in 1991 for a heterogeneous layer model under RF penetration (Haacke *et al* 1991). Later, experimental and simulation studies showed the strong dependence of the curvature of RF fields to the EP of the biological tissues (Alecci *et al* 2001, Yang *et al* 2002, Collins *et al* 2005, Vaidya *et al* 2016). Relatively recent studies have shown systematic methods to calculate EP from spatial variation of B_1^+ (the effective transmit RF field) in phantoms and animal tissue samples (Wen 2003, Katscher *et al* 2009, Bulumulla *et al* 2012, Zhang *et al* 2013b). Subsequently, simplified EPT reconstructions based only on B_1^+ phase or magnitude were introduced to reduce the imaging and computational time at 1.5 T (Voigt *et al* 2011) and 7 T (van Lier *et al* 2012a). In the simplified standard EPT approaches based on the Helmholtz equations, second order derivatives of the B_1^+ phase or magnitude are used to generate conductivity and permittivity maps, respectively (Van Lier *et al* 2014). More recently, other reconstruction approaches have been proposed to improve noise robustness of EP mapping (Bevacqua *et al* 2019, Leijsen *et al* 2019, Shin *et al* 2019, Serralles *et al* 2016, Gurler and Ider 2016, Li *et al* 2017, Motovilova *et al* 2015, Wang *et al* 2019a, Arduino *et al* 2018), and several studies have demonstrated application of EPT for clinical diagnosis (Katscher and van den Berg 2017, Katscher *et al* 2013a, Van Lier *et al* 2011, Huhndorf *et al* 2013, Gurler *et al* 2016, van Lier *et al* 2012b, Wang *et al* 2019b). Studies have shown novel contrast in the detection of cancer and tumor progression particularly by conductivity mapping (Kim *et al* 2016, Tha *et al* 2018, Balidemaj *et al* 2016, Liu *et al* 2017a, Shin *et al* 2015, Kim *et al* 2018). However, the more routine clinical use of permittivity as well as conductivity mapping is hampered by inaccuracy. As recent studies have shown, the inaccuracy in standard EPT techniques, especially with respect to permittivity mapping (Gavazzi *et al* 2019) is due to boundary issues (Jin

Keun Seo *et al* 2012, Duan *et al* 2016), limited signal-to-noise ratios (SNR) and spatial resolution (Shin *et al* 2015, Mandija *et al* 2017) at clinical field strengths. More specifically, because numerical approaches to solve the Helmholtz-based EPT equations utilize the Laplacian of the B_1^+ phase and magnitude maps, the EPT solution is very sensitive to the noise and low SNR of these maps, which can severely degrade the quality of EP maps (Lee *et al* 2015b, Michel *et al* 2014). These limitations have motivated the current study as a means to investigate the benefits of implementing Helmholtz-based EPT at 21.1 T. Interestingly, at the Larmor frequency of 900 MHz, most biological tissues (*e.g.* gray matter with σ = 0.94 S/m and ε_r = 52.72 (Gabriel 1996)) are between the extreme of $\omega\varepsilon_0\varepsilon_r >> \sigma$ for which a magnitude-only based permittivity estimation has increased accuracy and $\sigma >> \omega\varepsilon_0\varepsilon_r$ for which the phase-only conductivity has increased accuracy (Seo *et al* 2014). As EPT at 21.1 T falls in this intermediate regime, it was necessary to determine if conventional EPT approaches are adequate to produce reasonable and spatially resolved estimates of conductivity and permittivity for preclinical specimen. Although higher field strengths can provide better SNR as well as higher spatial resolution and effects of EP on the B_1^+ may be more pronounced, the feasibility and accuracy of implementing the Helmholtz-based EPT approach at higher preclinical fields needs to be investigated. Indeed, for clinical MR scanners, a comparison study between fields of 1.5, 3 and 7 T has shown the tradeoff between SNR improvement and validity of B_1^+ phase approximation (Van Lier *et al* 2014).

Testing the assumptions intrinsic to Helmholtz-based EPT, this study aimed to compare the precision of Phase-based versus Full-form conductivity mapping at 21.1 T using phantoms, *ex vivo* and *in vivo* rat brains. For phantoms, the comparison is extended to two different coils: a linear birdcage and a quadrature saddle coil to investigate the effect of coil structures and operational modes on conductivity estimation at 900 MHz. Additionally, the possibility of generating permittivity maps using Magnitude-based and Full-form reconstructions are investigated in both phantoms and rat brain. As a case study, different EPT approaches were applied to an *in vivo* rodent model of transient cerebral ischemia to investigate sensitivity to conductivity and permittivity alterations.

Methods

Dielectric Probe Measurements and Phantom Design

Four test solutions containing different sodium chloride (NaCl) concentrations (0, 4.7, 11.7 and 25.6 g/L) dissolved completely in ultra-purified water were evaluated. $CuSO_4$ (0.15 g/L) was added to each solution to reduce relaxation, yeilding T_1 values between 1.7-1.8 s with T_2 values between 520-675 ms over the full range of the saline solutions used. Conductivity and permittivity were measured for each of the solutions using an HP Dielectric Probe (HP 85070B, Keysight Technologies, Santa Rosa, CA). The dielectric probe had a shield diameter of 1.6 cm and center conductor diameter of 0.9 mm. All measurements were conducted in 50-mL beakers to satisfy the width and depth required by this dielectric probe. According to the probe manufacturer, the accuracy of the permittivity measurement is ±5% (corresponding to a worst case of $\Delta\varepsilon_r < \pm 4$ for the solutions used), and the accuracy of the loss tangent, tan δ, is ±0.05 (corresponding to a worst case of $\Delta\sigma < \pm 0.19$ for the ε_r of solutions used). For calibration at 900 MHz, the AC conductivity of ultra-purified water without $CuSO_4$, found by dielectric probe measurements was 0.14 S/m with relative permittivity of 79, which agrees with the theoretical conductivity (σ_w=0.19) calculated from the Debye dielectric relaxation and Cole-Cole (α=0) models for water at 25 C at this frequency with $\varepsilon_w(0)$=78.36, $\varepsilon_w(\infty)$=5.2 and τ_w=8.27 ps (Kaatze 1997). Note, as 900 MHz enters the microwave regime, the frequency-dependent water conductivity is non-zero. Used as the ground-truth for MR experiments, the conductivities and permittivities measured in this fashion for each solution were tabulated (Tables 1 and 3), with the mean sand standard deviations calculated from five individual measures at 900 MHz.

For MR experiments, 3 mL of each of the four test solutions were placed in four separate transfer pipettes with diameters of 1.4 cm, filling a length of 4 cm. The pipettes containing the aforementioned NaCl concentrations were labeled as tubes 1-4, respectively. Pipettes were inverted such that the thin-walled pipette bulbs (wall thickness of 0.34 mm) could be placed simultaneously within a 3-cm cylindrical container that was filled with the solution of tube 1. This arrangement permitted multiple solutions to be positioned and scanned simultanouesly within the 33-mm diameter of an *in vivo* rat head coil and confines of a vertical bore, 900-MHz magnet. Although geometrically different from biological specimens, this phantom covered a range of biologically relevant conductivities and permittivities, and follows the phantom design used widely by others (Zhang *et al* 2013a, Lee *et al* 2015c) as an accessible means of testing the EPT reconstruction. Notably, tubes 2 and 3 provide conductivities that cover the range of gray matter (σ = 0.94 S/m) and cerebrospinal fluid (σ = 2.4 S/m) of the human brain at 900 MHz (Gabriel 1996). It also should be noted that at the operating frequency of 900 MHz, the RF penetration through the thin plastic wall is significant, and though an image discontinuity is present, the wall appears transparent to the RF and should not impact the EPT calculations beyond the boundary/image discontinuity. However, DC or conduction currents will be interrupted by even this thin insulating wall thickness (Kwon *et al* 2014). More biologically relevant assessments were performed on the *ex* and *in vivo* rat brain specimens described below for comparison.

Data Acquisition

Data were acquired at the National High Magnetic Field Laboratory using a 21.1-T (^{1}H frequency of 900 MHz) vertical magnet (Fu *et al* 2005) equipped with an Avance III spectrometer

(Bruker BioSpin, Billerica, MA, USA) and ParaVision software. The 900-MHz system is an ultra-widebore magnet with a diameter of 10.5 cm and gradient bore size of 6.35 cm. The gradient system (Resonance Research Inc., Billerica, MA, USA) can produce magnetic field gradients up to 600 mT/m in all directions, with a rise time of 120 μs. Two home-built RF coils (Figure 1) constructed on a 33-mm diameter former were used for both transmission and reception: 1) a linear sliding ring $^{1}H/^{23}Na$ birdcage coil (Qian *et al* 2012); and 2) a ^{1}H saddle coil driven in quadrature mode (Muniz *et al* 2011, Rosenberg *et al* 2017). For the ^{1}H saddle coil, the most homogenous region of the coil was matched to the size of one tube; therefore, conductivities using both EPT approaches were investigated by rotating the phantom inside the coil and acquiring separate data with each tube centered within this homogenous FOV. For phantom acquisitions, the temperature was kept at 25 C in the MR scanner using a regulated water supply.

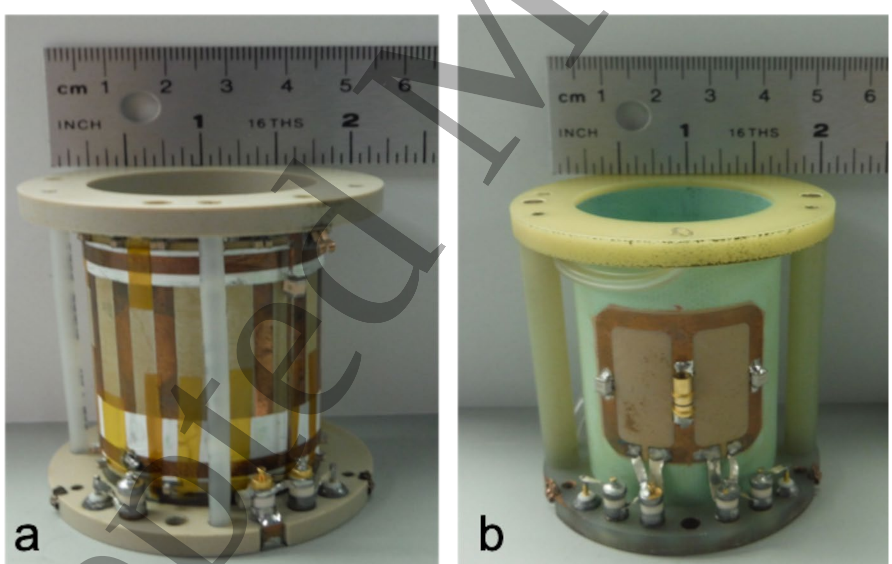

Figure 1. RF coils: **a)** $^{1}H/^{23}Na$ birdcage coil; **b)** ^{1}H saddle coil

Two measurements were acquired for EPT: one to map the B_1^+ magnitude and another to determine the B_1^+ phase, both using a spin-echo (SE) acquisition from the conventional Bruker pulse sequence library (see supplemental data, Figure 1). The B_1^+ magnitude map was generated using a double angle method (DAM) (Stollberger and Wach 1997, Cunningham *et al* 2006) without preparation in which the initial excitation was either α_1=60° or α_2=120° with a 180° refocusing pulse. The ratio of the signal intensities ($R=I_{\alpha 2}/2I_{\alpha 1}$) was used to calculate the flip map ($\alpha = \cos^{-1} R$), which was then converted to the $|B_1^+|$ map. For the B_1^+ phase measurement, a SE image was acquired with a 90° initial excitation. As the resultant transceive phase image is the summation of both $B_1^+$and B_1^- phases, the transceive phase assumption was utilized to calculate the B_1^+ phase map as half of the measured transceive phase (Overall *et al* 2010, van Lier *et al* 2012a). For both B_1^+ phase and magnitude measurements, multi-slice 2D spin SE sequences were acquired with a TE/TR=15/2000 ms, resolution of 0.13 x 0.13 mm^2 for a field of view of 34 x 34 mm^2 and matrix size of 256 x 256 for phantoms. Nine slices were acquired in an axial direction with a slice thickness of 1 mm using a 6-ms three-lobe sinc excitation pulse. Trapazoidal crushers (10% maximum gradient strength with a 1-ms total duration) were applied before excitation and around the slice selection gradient applied to the 180 pulse to eliminate spurious signals and stimulated echoes. The SE sequence helped to exclude phase contributions from off-resonance effects, including susceptibility distortions. For phantom measurements, no eddy current correction was utilized, although compensated tests were performed subsequently to assess the impacts of eddy currents (see supplemental data, Figure 2). These eddy current correction tests of the phantom demonstrated less than an average 17% and 11% difference in the standard deviation and 13% and 9% in the RMSE of conductivity and permittivity, respectively. These variations were deemed negibile for the phantom, and thus eddy current correction was not persued. However, biological specimen (*ex* and *in vivo*) demonstrated potential eddy current impacts, necessitating correction as indicated below. In addition to the SE EPT measurements, a gradient-recalled echo (GRE) sodium image was acquired with TE/TR=1.18/300 and 4 averages using the $^{1}H/^{23}Na$ birdcage to confirm the position and relative salinity of the tubes in the coil.

Ex *and in vivo measurements*

To show the feasibility of the technique in animal models, data also were acquired from naïve preserved and ischemic stroke rats at 21.1 T.

***Ex vivo* sample preparation:** Under anesthesia, two juvenile (~40-day-old) naïve male Sprague-Dawley rats (~200 g) were transcardially perfused with phosphate buffered saline and then 4% paraformaldehyde. Intact heads were harvested using a guillotine and immersed in 4% paraformaldehyde for at least 24 h. Prior to any imaging session, the preserved rat heads were transferred to phosphate buffered saline and washed for at least 24 h to remove excess fixative from the tissue. Before imaging, the heads were immersed in a non-protonated fluorocarbon (FC-43, 3M Corp, Minneapolis, MN) to provide susceptibility matching during MRI (Webb and Grant 1996).

***In vivo* stroke model:** In accordance with the FSU Animal Care and Use Committee, an ischemic stroke was introduced by a transient middle cerebral artery occlusion (MCAO) in a single juvenile male Sprague-Dawley rat (200 g, ~40 days old) as described previously (Longa *et al* 1989). Briefly, the internal carotid artery and external carotid artery were exposed, and a rubber-coated filament (Doccol, Sharon, MA) was placed into the external carotid artery and guided 1.9 cm into the ICA until the middle cerebral artery was blocked. Occlusion was sustained for 1.5 h, followed by re-anesthetization and removal of the filament. The MCAO animal was imaged *in vivo* at 24 h following the occlusion using the $^{23}Na/^{1}H$ double-tuned birdcage RF coil discussed above. It was positioned and secured in the RF coil through the use of a bite bar, which also delivered gaseous anesthesia. Hip and girdle straps restrained the lower body of the animal as MRI experiments at

21.1 T are conducted with the rat in a heads-up, vertical position. The rat was induced with 3% isoflurane in 100% O_2, and maintained on 1-2% isoflurane through experimentation. Respiration was monitored, and acquisitions were triggered using a pneumatic pillow and animal monitoring system (SA Instruments, Inc., Stony Brook, NY).

To achieve *ex* and *in vivo* imaging times of 15 min, the acquisition matrix was reduced to 128x128, and a fast spin echo (FSE) with an acceleration RARE factor of four was utilized to generate B_1^+ magnitude maps from the DAM technique described above as well as the B_1^+ phase. The temperature was kept at 30 C in the MR scanner using a regulated water supply. Additionally, unlike phantom experiments, there was evidence of eddy current phase artifacts in the rat brain (Figure 2) similar to those identified previously (van Lier *et al* 2012a) as a decreasing phase superimposed on the overall phase map. Therefore, to eliminate the potential impact of eddy currents, the average phase from two opposite readout directions was used (Bernstein *et al* 2004, van Lier *et al* 2012a). All other data acquisition parameters were kept the same as the phantom imaging methods detailed above. In addition to ^{1}H MRI, ^{23}Na *in vivo* images were acquired in 23.5 min using a 3D ^{23}Na GRE sequence with 36 averages, TE/TR = 1.05/50 ms, FOV of (40 mm)^3 and matrix of 40x40x40. The sodium MRI datasets were zero-filled to an image matrix of 64x64x40 to yield an image resolution of 0.625x0.625x1.0 mm^3, and partition positions were matched to those used for ^{1}H EPT acquisitions.

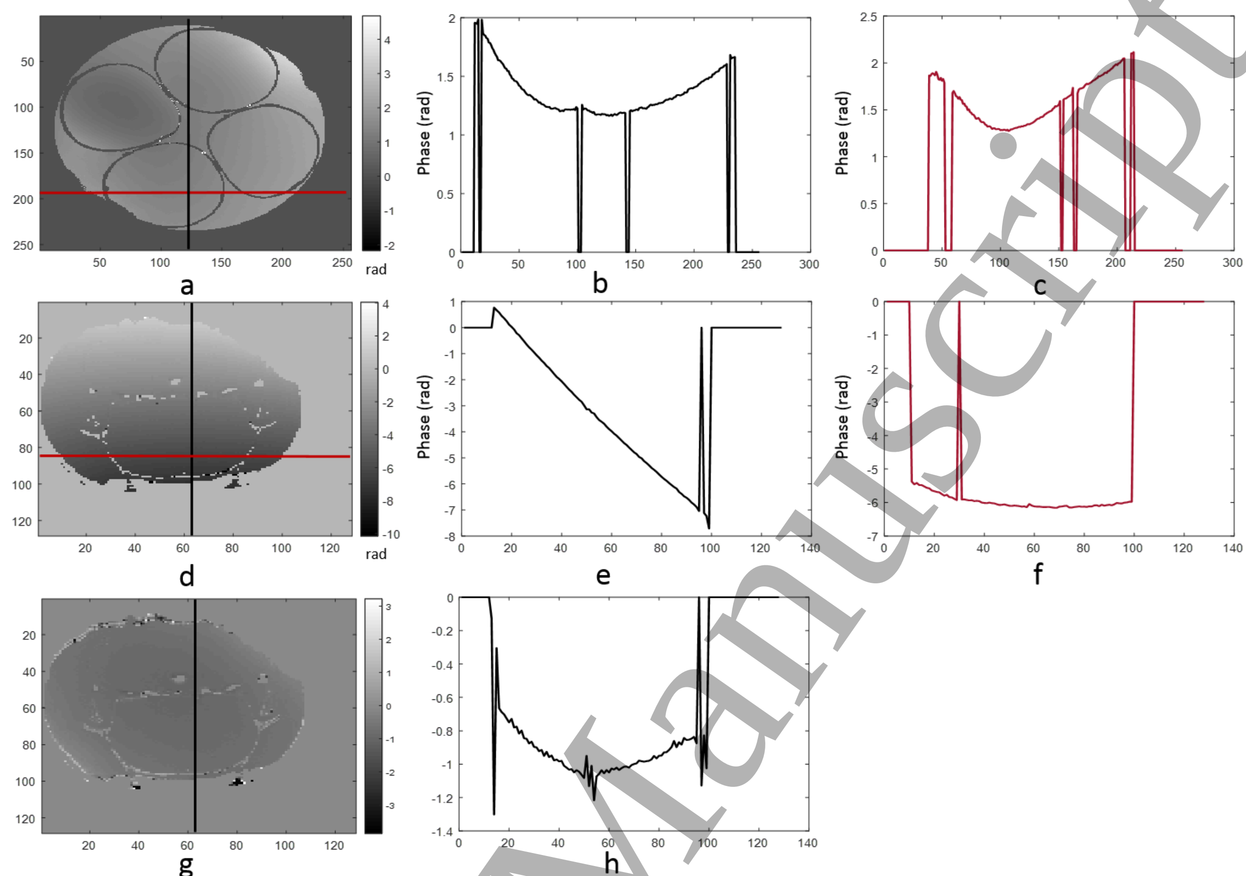

Figure 2. Phase distribution in x and y directions for phantom and rat brain specimens. **a)** Unwrapped phase image from the phantom displays a point localized within tube 2 that is subsequently delineated by vertical (black) and horizontal (red) phase lines displayed in **b)** and **c)**, respectively. **d)** Unwrapped phase image from an *ex vivo* sample displaying a point subsequently delineated by vertical (black) and horizontal (red) phase lines displayed in **e)** and **f)**, respectively. The drop in phase shown in e), which previously has been attributed to eddy currents (van Lier *et al* 2012a), required the use of eddy current correction for all rat brain specimens. Using reversal of the readout gradient in a subsequent scan and averaging the phase of the two scans, an eddy current corrected phase map was utilized for EP reconstructions. Shown in **g)** the corrected phase image and **h)** the corrected phase line correspond to (d) and (e), respectively.

EP reconstruction

A Helmholtz-based EPT technique also called standard EPT (Voigt *et al* 2011, van Lier *et al* 2012a, Ammari *et al* 2015, Van Lier *et al* 2014) was used to calculate conductivity (σ) and relative permittivity (ε_r). Based on this technique, EP can be calculated for regions with piecewise constant EP from the B_1^+ field using the homogenous Helmholtz equation:

$$\nabla^2 B_1^+ \approx -\omega\mu_0\kappa B_1^+ \quad [1]$$

where $\kappa = \varepsilon_r\varepsilon_0\omega + i\sigma$, ω is the Larmor frequency, μ_0 and ε_0 are the vacuum permeability and permittivity, respectively. To calculate σ, the imaginary part of Eq. 1 was extracted, and Eqs. 2 and 3 were used for Full-form and Phase-based approach, respectively:

$$\sigma_{FF} = \frac{1}{\mu_0\omega}\nabla^2\varphi^+(\mathrm{r}) + \frac{2\nabla|B_1^+|\cdot\nabla\varphi_1^+(r)}{\omega\mu_0|B_1^+|} \quad [2]$$

and

$$\sigma_{PO} \approx \frac{1}{\mu_0\omega}\nabla^2\varphi^+(\mathrm{r}). \quad [3]$$

The Full-form approach requires both the amplitude and phase of complex transmit field $B_1^+ = |B_1^+|\exp(-i\varphi^+)$. However, if the second term of Eq. 2 is much smaller than the Laplacian of the phase, the first term dominates. In the phase-based approach, only the contribution of this dominant term in the estimated conductivity is considered.

To calculate ε_r, the real part of Eq. 1 was extracted, and Eqs. 4 and 5 were used for the Full-form and Magnitude-based approach, respectively:

$$\varepsilon_r = \left(\frac{(\nabla\varphi_1^+)^2}{\omega^2\mu_0\varepsilon_0} - \frac{\nabla^2(|B_1^+|)}{\omega^2\mu_0\varepsilon_0|B_1^+|}\right) \quad [4]$$

and

$$\varepsilon_r \approx \left(-\frac{\nabla^2(|B_1^+|)}{\omega^2\mu_0\varepsilon_0|B_1^+|}\right). \quad [5]$$

In the Magnitude-based permittivity approach, it is assumed that permittivity can be estimated by only considering the dominant term, which is the Laplacian of the magnitude of the B_1^+. In this study, the accuracy of these simplified methods is compared to the Full-form approaches at the frequency of 900MHz.

In-house MATLAB® (The MathWorks Inc., Natick, MA) scripts were used to calculate conductivity and permittivity from the above equations. Phase unwrapping by Goldstein's method (Goldstein *et al* 1988) was included in post-processing of the phase. To compensate for the inherent noise amplification of Laplacian operation in later steps, B_1^+ magnitude and phase were smoothed with a moving average filter of 6×6 pixels. Additionally, the Laplacian kernels applied to the data incorporate a Gaussian filter as part of the numerical calculation. The Laplacian for both conductivity and permittivity was calculated by convolution with a large noise-robust kernel L of 5×7 presented below:

$$L_x = \begin{bmatrix} 1 & 2 & -1 & -4 & -1 & 2 & 1 \\ 4 & 8 & -4 & -16 & -4 & 8 & 4 \\ 6 & 12 & -6 & -24 & -6 & 12 & 6 \\ 4 & 8 & -4 & -16 & -4 & 8 & 4 \\ 1 & 2 & -1 & -4 & -1 & 2 & 1 \end{bmatrix} = L_y^T$$

and

$$L_z = \begin{bmatrix} 0.5 & 0 & -1 & 0 & 0.5 \\ 1 & 0 & -2 & 0 & 1 \\ 0.5 & 0 & -1 & 0 & 0.5 \end{bmatrix}$$

The matrix is extrapolated based on noise-robust kernels published previously (van Lier *et al* 2012a, Holoborodko 2009). The Laplacian of the B_1^+ phase or magnitude was calculated in the plane by summing the result of convolving data with kernel L_x to determine the x component and its transpose (L_y) to determine the y component, yielding a symmetric matrix (7×7) in-plane (Mandija *et al* 2017). Given the reduced number of slices in the z-direction, a small kernel of 3×5 was employed in that direction. Notably, for phantom calculations, the Laplacian of the phase along the direction of the slice selection gradient was close to zero due to symmetry along the tubes, yielding a negligible z component of the Laplacian. Although more noise robust, these larger kernels are susceptible to boundary errors as more pixels in transitional regions are affected.

Imaging Data Analysis

Conductivity and permittivity values were determined for phantom, *ex* and *in vivo* measurements based on regions of interest (ROI) analysis for which the means and standard deviations of all pixels within the boundaries of the ROI were calculated. For phantom experiments, EP values (Tables 1 and 3) were calculated from ROI centered in each tube and applied across the five middle slices of the slice package; ROI were chosen to exclude the boundary regions where computational artifacts dominate. In general, ROI placement avoided the 15 pixels nearest the tube periphery to minimize boundary artifacts. Based on this ROI analysis, statistical significance was determined between and within reconstruction and acquisition approaches using a one-way ANOVA with Tukey's HSD post-hoc test ($p<0.05$). To compare each reconstruction approach further, the mean differences and root mean square errors (RMSE) were calculated for all pixels within the ROI for conductivity (Table 2) and permittivity (Table 3) separately. The RMSE was calculated using:

$$RMSE = \sqrt{N^{-1} \sum_{n \leq N} (x_n - \bar{x})^2}, \qquad [6]$$

where $\bar{x}$ is the target conductivity or permittivity measured by the dielectric probe, x_n is the estimated conductivity or permittivity for the n^{th} pixel, and *N* represents all pixels from the ROI. In addition, a linear regression (Figure 5) was performed on calculated EP values relative to dielectric probe values for each approach to determine the degree of correlation by means of a Pearson's coefficient.

For *ex* and *in vivo* measurements, ROI were placed on central slices to calculate the pixel mean and standard deviation of conductivity and permittivity for the two reconstruction approaches using only linear birdcage acquisitions. Referenced to the corpus callosum on magnitude MRI, the EP ROI were located in a single slice transecting the striatal region of the *ex vivo* brain (Figure 6 and Table 5). For the *in vivo* case modeling ischemic stroke, two slices were analyzed (Figure 7). First, in a slice centered within the ischemic region, the striatum again was analyzed using ipsi- and contralateral placement of EP ROI referenced to the corpus callosum. Second, in a slice distal to the ischemic lesion, left and right hemisphere ROI were placed within the hippocampus. For all *in vivo* ROI (Table 6), care was taken to avoid the ventricles and major white matter tracks, effectively limiting the EP analysis to gray matter while maintaining central ROI placement to avoid boundary artifacts resulting from the reconstruction.

Results

Figure 3 displays the ^{1}H magnitude MR image, the $|B_1^+|$ map, the unwrapped transceive phase map, Full-form and Phase-based generated conductivity reconstructions as well as the Full-form and Magnitude-based relative permittivity reconstructions. All data shown are from the middle slice of the slice package for the linear birdcage coil. Figure 3a) acquired using a SE sequence shows loss of signal at the feed points of the linearly excited birdcage, which are adjacent to tubes 2 and 3. Except for these points, RF homogeneity is uniform in the volume birdcage as evident in Figure 3b). For the quadrature saddle coil, Figure 4 displays data acquired from each tube (1-4) positioned within the limited FOV of the saddle coil by rotating the phantom. Quadrature detection provided a 50% increase in SNR over the linear birdcage coil. However, the coil has a less uniform RF field as demonstrated in the line plots of Figure 4, with the $|B_1^+|$ and transceive phase dropping off as a function of the distance from the face of the saddle coil.

Table 1 displays mean conductivities and standard deviations for each coil configuration and EPT reconstruction. Served as a ground truth, conductivity and permittivity values for solutions measured with the dielectric probe are also presented in Table 1. Table 2 provides the percent error difference with respect to the dielectric probe and RMSE for each coil configuration and EPT approach. Relative permittivities for both Full-form and Magnitude-based reconstruction of the phantom in the birdcage coil are presented in Table 3 using the same ROI as conductivity measurements. The percent error and RMSE of the relative permittivities are reported in Table 4.

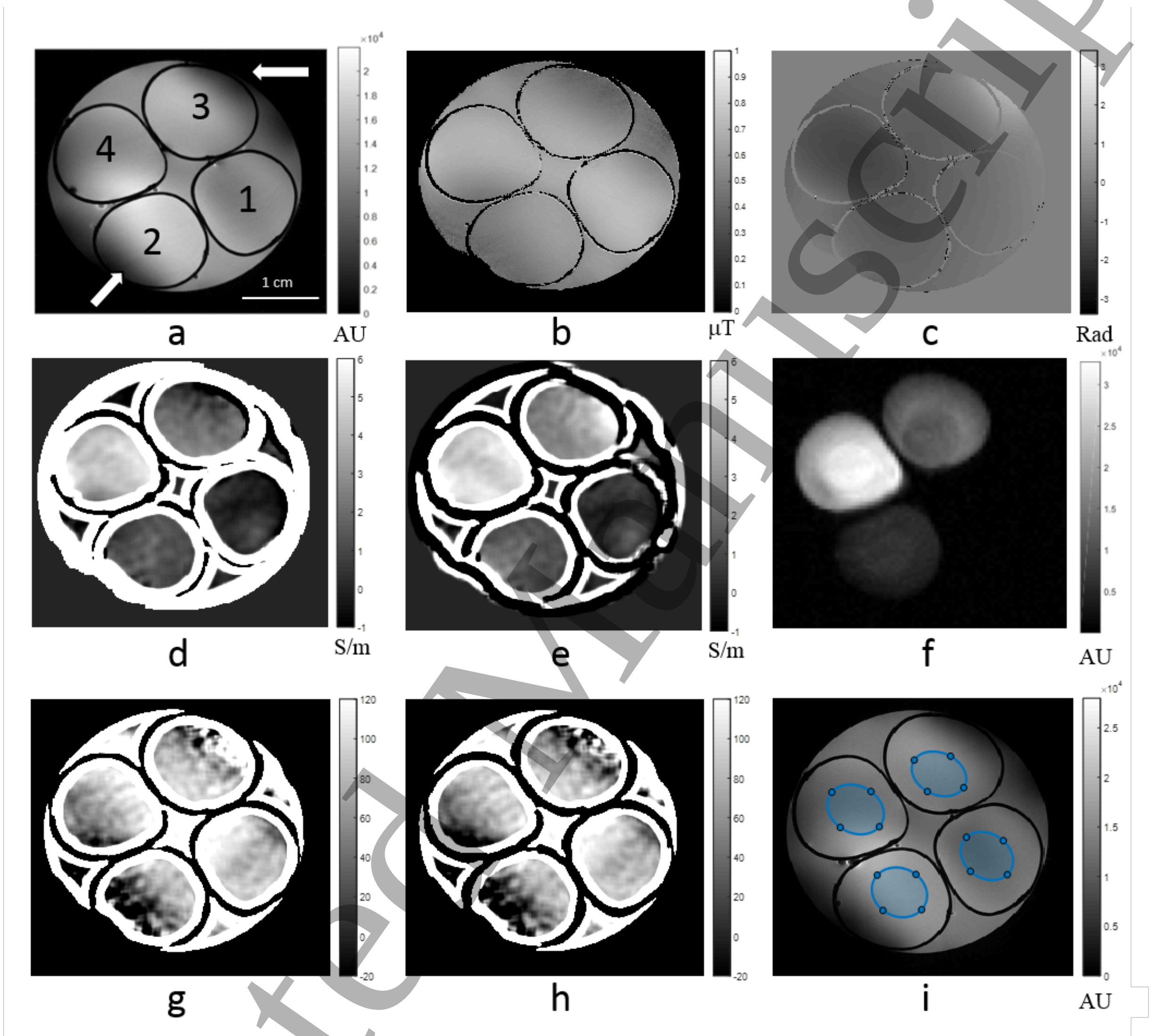

Figure 3. Phantom with tube 1 = 0.21 S/m, tube 2 = 1.01 S/m, tube 3 = 2.04 S/m and tube 4 = 4.08 S/m in the birdcage coil: **a)** ^{1}H MR image displaying tube numbers (arrows point to the RF feed and ground points); **b)** B_1^+ magnitude map; **c)** Phase image; **d)** Full-form conductivity (S/m); **e)** Phase-based Conductivity (S/m); **f)** ^{23}Na MR image; **g)** Full-form relative permittivity; **h)** Magnitude-based relative permittivity; **i)** ^{1}H MR image showing positioning of ROI for quantification.

Figure 5 (a) shows plots of calculated mean conductivities from any of the approaches versus the ground truth. Regression analysis of this data yielded linear fits with all R^2 values greater

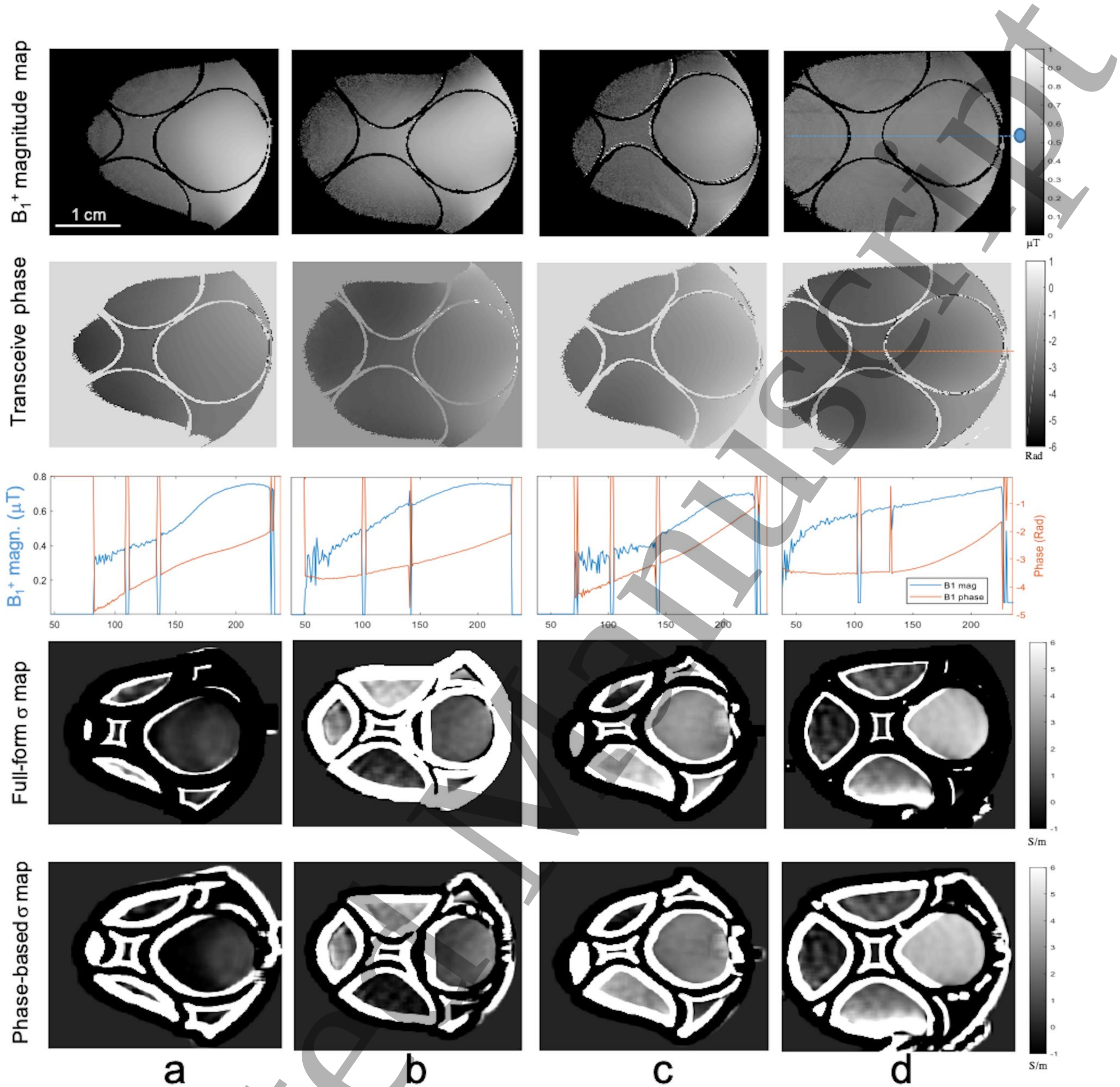

Figure 4. Phantom in the quadrature saddle coil: columns a through d correspond to positioning of tube 1=0.21 S/m, tube 2 = 1.01 S/m, tube 3 = 2.04 S/m and tube 4 = 4.08 S/m, respectively, in the saddle coil FOV. Row 1 images correspond to the B_1^+ magnitude map, the blue dot on the upper right image shows the position of the coil. Row 2 images provide the transceive phase; Row 3 plots display the middle lines (element 128 of the matrix) from the B_1^+ magnitude map (red) and transceive phase (blue) as a function of pixel distance from the coil surface. Rows 4 and 5 are the conductivity maps generated from the Full-form and Phase-based reconstructions, respectively. All the images are masked with 6% threshold.

than 0.96 and Pearson's linear correlation coefficients greater than 0.98 for all reconstruction approaches indicating that measured conductivities from each approach are in good correlation with the ground truth. Similarly, Figure 5b) shows plots of calculated mean permittivities versus the ground truth. Regression analysis of this data yielded linear fits with R^2 values of 0.97 and Pearson's linear correlation coefficients of 0.99 for both methods indicating that measured permittivities are in excellent correlation with the ground truth.

Table 1. Conductivity (Mean ± SD) calculated by different EPT reconstruction approaches and dielectric probe measurements. Within a reconstruction approach for a given RF coil, significance ($p<0.05$) was found between all of the samples using a one-way ANOVA with Tukey's HSD post-hoc test.

	Dielectric Probe	Linear Birdcage Coil		Quadrature Saddle Coil	
Different salinities	Average Conductivity at 900 MHz (S/m)	Full-form EPT Conductivity (S/m)	Phase-based EPT Conductivity (S/m)	Full-form EPT Conductivity (S/m)	Phase-based EPT Conductivity (S/m)
Tube 1 (0 g/L)	0.20 ± 0.003	0.27 ± 0.46	0.42 ± 0.49	0.64 ± 0. 32	0.56 ± 0. 32
Tube 2 (4.7 g/L)	1.01 ± 0.001	1.32 ± 0.31	1.37 ± 0.36	1.66 ± 0.27	1.54 ± 0.35
Tube 3 (11.7 g/L)	2.04 ± 0.001	2.31 ± 0.35	2.78 ± 0.33	3.09 ± 0.20	2.32 ± 0.21
Tube 4 (25.6 g/L)	4.08 ± 0.002	4.51 ± 0.28	4.61 ± 0.31	4.42 ± 0. 21	4.27 ± 0.23

Table 2. Percent Error to Dielectric Probe conductivity and Root Mean Square Error (RMSE) for different conductivity reconstruction approaches.

	Linear Birdcage Coil				Quadrature Saddle Coil			
Different salinities	Full-form Conductivity		Phase-based Conductivity		Full-form Conductivity		Phase-based Conductivity	
	Percent Error	RMSE (S/m)	Percent Error	RMSE (S/m)	Percent Error	RMSE (S/m)	Percent Error	RMSE (S/m)
Tube 1 (0 g/L)	35%	0.46	110%	0.55	220%	0.55	180%	0.48
Tube 2 (4.7 g/L)	31%	0.42	36%	0.58	64%	0.71	52%	0.64
Tube 3 (11.7 g/L)	13%	0.45	36%	0.88	51%	1.06	14%	0.35
Tube 4 (25.6 g/L)	11%	0.53	13%	0.61	8%	0.41	5%	0.28

Table 3. Relative permittivity (Mean ± SD) calculated by Full-form, Magnitude-based reconstruction and dielectric probe measurements. For EPT reconstructions, significance (*p<0.05) was found between tube 4 and all other samples using a one-way ANOVA with Tukey's HSD post-hoc test. The only other significant difference was found between tubes 1 and 3 at the ^p=0.05 level.

	Dielectric Probe	Linear Birdcage Coil	
Different salinities	Average Permittivity at 900 MHz	Full-form Relative Permittivity	Magnitude-based Relative Permittivity
Tube 1 (0 g/L)	78.74 ± 0.14	86.93 ± 10.03	83.25 ± 09.91^
Tube 2 (4.7 g/L)	77.66 ± 0.01	85.00 ± 13.40	82.81 ± 13.03
Tube 3 (11.7 g/L)	76.13 ± 0.06	81.95 ± 09.12	77.49 ± 10.88^
Tube 4 (25.6 g/L)	73.41 ± 0.05	72.04 ± 13.03*	69.44 ± 12.83*

Table 4. Percent Error to dielectric probe permittivity and Root Mean Square Error (RMSE) for different permittivity reconstruction approaches.

Different salinities	Full-form Relative Permittivity		Magnitude-based Relative Permittivity	
	Percent Error	RMSE	Percent Error	RMSE
Tube 1 (0 g/L)	10%	12.59	6%	11.02
Tube 2 (4.7 g/L)	9%	15.53	7%	13.98
Tube 3 (11.7 g/L)	8%	10.66	2%	10.66
Tube 4 (25.6 g/L)	2%	13.21	5%	13.21

Statistical analysis identified a unique and significantly different value for each conductivity as a function of the salinity within a given reconstruction approach and RF coil configuration. On the other hand and independent of the reconstruction method, permittivity values for the highest salinity sample (tube 4) were the only measures found to be consistently and significantly different from the other tubes (1-3). This finding was anticipated for an otherwise high dielectric phantom requiring a large addition of NaCl to induce losses and reduce the permittivity, as reflected in dielectric probe measurements. Additional statistical analysis is provided in the supplemental information (see supplemental data).

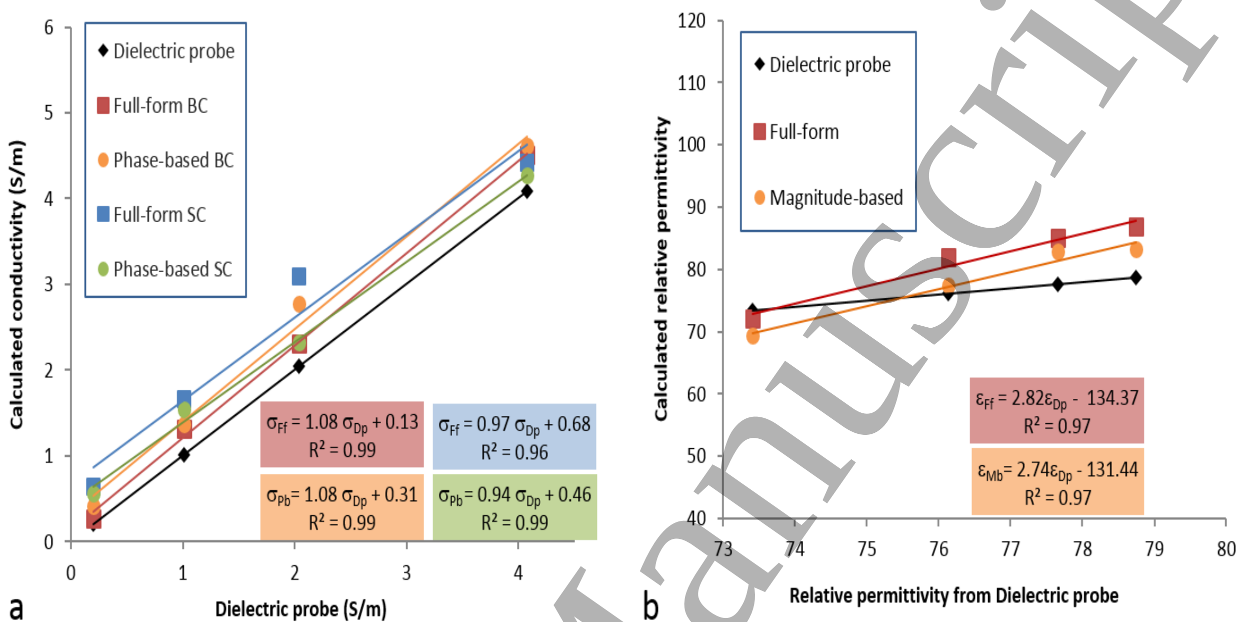

Figure 5. **a)** Mean conductivities from linear birdcage and quadrature saddle coils for Full-form and Phase-based approaches as compared with dielectric probe values; **b)** Mean relative permittivities from linear birdcage coil for Full-form and Magnitude-based approaches as compared with dielectric probe values. Lines represent linear regression fits of the dielectric probe measurements for each EPT reconstruction and coil configuration.

Ex vivo conductivity and permittivity maps from both reconstruction techniques are displayed in Figure 6 for a middle slice of a preserved rat brain. Calculated conductivity and permittivity values for the two ROI shown in Figure 6 are presented in Table 5. Figure 7 displays the *in vivo* result from the MCAO rat for two representative slices of the brain. One slice is selected within the stroke region and another slice distal to the ischemic lesion. Measured conductivity and permittivity for the two ROI, one placed in each hemisphere, for the two slices are shown in Table 6. The ipsilateral ROI was selected in reference to the corpus callosum (namely below this structure) to avoid boundary artifacts but still represent the center of the ischemic lesion and be largely devoid of white matter tracts. Its contralateral compliment and the ROI of the distal slice are matched in size and central location for comparison. ^{23}Na MRI images are also provided in

Figure 7 (d) to illustrate the increase of sodium signal at 24 h post MCAO in the ischemic lesion versus the contralateral side.

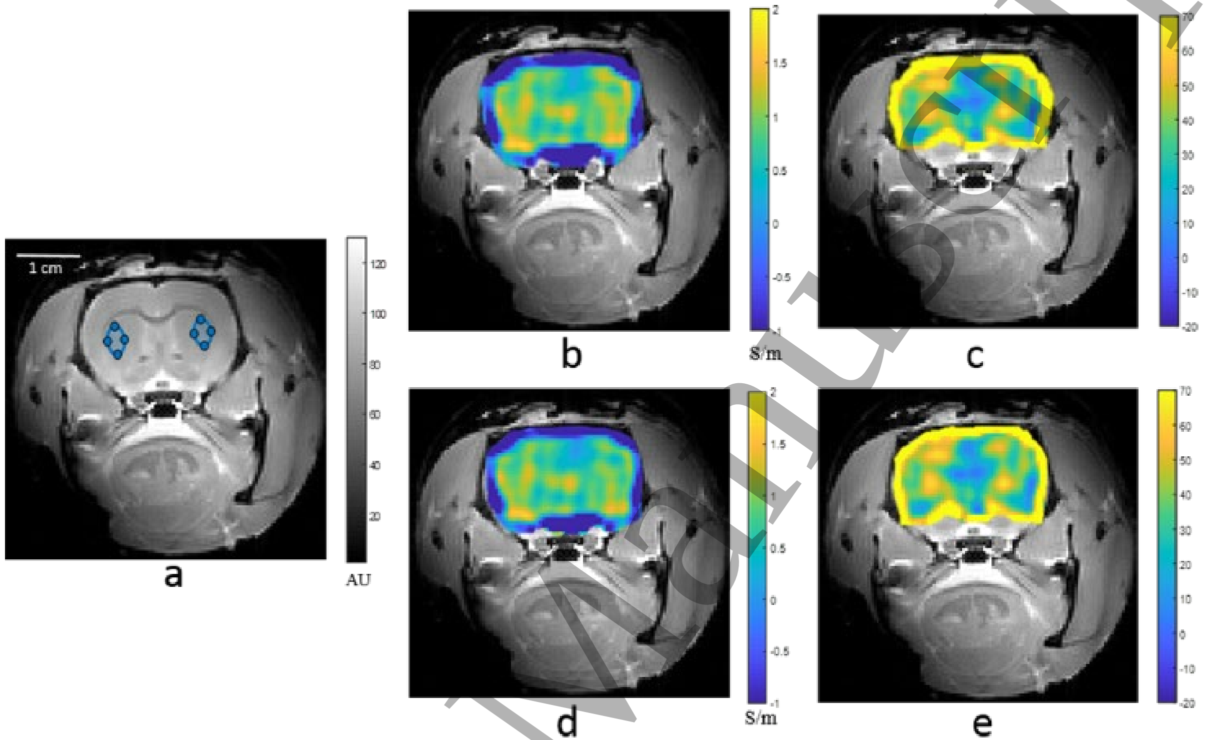

Figure 6. *Ex vivo* rat brain: **a)** [1]H MR image also displaying the ROI; **b)** Full-Form conductivity; **c)** Full-form relative permittivity **d)** Phase-based conductivity; **e)** Magnitude-based relative permittivity.

Table 5. Means and standard deviations for relative permittivity and conductivity measurements in the *ex vivo* brain.

ROI Left			
Conductivity (S/m)		Relative Permittivity	
Full-form	Phase-based	Full-form	Mag-based
0.93 ± 0.17	1.01 ± 0.17	57.11 ± 4.43	56.38 ± 4.44
ROI Right			
Conductivity (S/m)		Relative Permittivity	
Full-form	Phase-based	Full-form	Mag-based
0.71 ± 0.19	0.92 ± 0.17	60.76 ± 5.93	58.86 ± 5.90

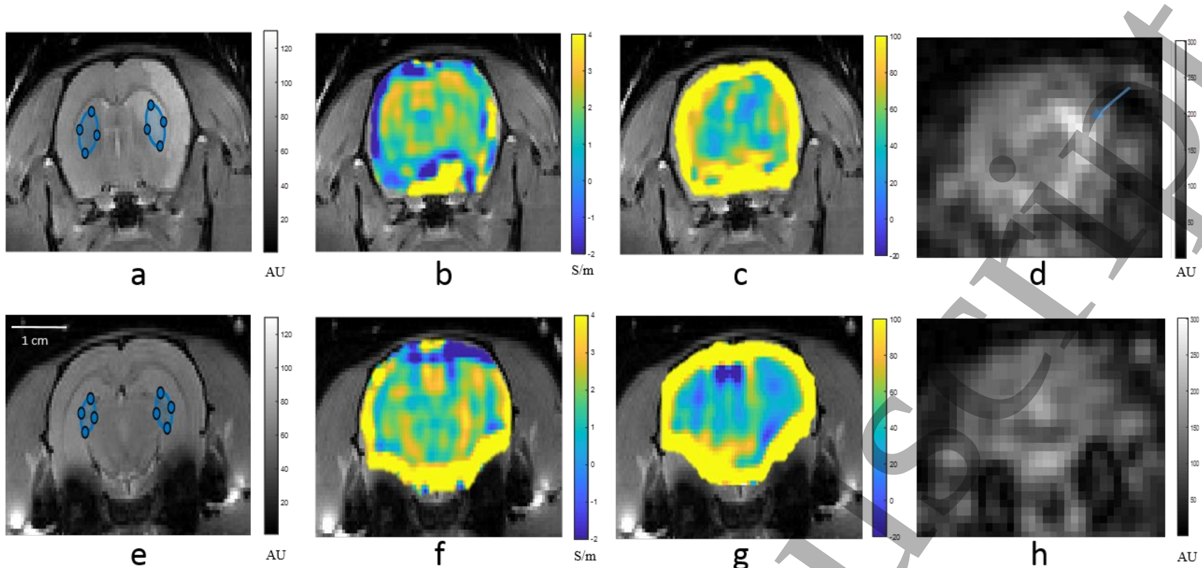

Figure 7. Two slices of *in vivo* rat brain, the top row is for a slice central to the ischemic lesion, bottom row is a slice distal to the lesion. **a)** ^{1}H image through the center of lesion displaying ROI placement **b)** Central Phase-based conductivity; **c)** Central Magnitude-based relative permittivity; **d)** ^{23}Na image with arrow designating the ischemic hyperintensity; **e)** Distal ^{1}H image displaying ROI placement; **f)** Distal Phase-based conductivity; **g)** Distal Magnitude-based relative permittivity; **h)** Distal ^{23}Na image displaying no sodium abnormalities.

Table 6. Pixel mean and standard deviations for relative permittivity and conductivity measurements in the *in vivo* brain.

Slice position to lesion	ROI Left			
	Conductivity (S/m)		Relative Permittivity	
	Full-form	Phase-based	Full-form	Mag-based
Central	1.23 ± 0.36	1.29 ± 0.38	40.91 ± 5.13	39.66 ± 5.18
Distal	1.19 ± 0.17	1.20 ± 0.16	40.12 ± 7.10	39.02 ± 7.38

Slice position to lesion	ROI Right			
	Conductivity (S/m)		Relative Permittivity	
	Full-form	Phase-based	Full-form	Mag-based
Central	1.64 ± 0.22	1.91 ± 0.23	64.15 ± 6.67	61.42 ± 6.35
Distal	0.96 ± 0.41	1.21 ± 0.42	40.47 ± 6.70	37.72 ± 6.83

Discussion

Higher magnetic fields necessitate application of a higher frequency B_1^+ field to match the Larmor resonance frequency condition of target nuclei. As a result, sample size becomes non-negligible to the RF wavelength, and sample EP and geometry influence B_1^+ field curvature. At 21.1 T (900 MHz), for which the B_1 wavelength $\left(\lambda = \frac{\lambda_0}{\sqrt{\varepsilon_r}}\right)$ in pure water ($\varepsilon_r \sim 80$) is 3.7 cm, B_1^+ fields generated by the RF coils (~3-cm diam.) interact strongly with the sample, and the field uniformity is highly influenced by the geometry and EP of the sample as well as the coil configuration (Amouzandeh *et al* 2018). On one hand, this coupling helps the detection of EP using Helmholtz-based EPT due to higher RF field curvature. On the other hand, it increases the difference between B_1^+ and B_1^- phases, impacting the validity of the transceive assumption used in EPT reconstructions (Katscher *et al* 2009, Balidemaj *et al* 2015). However, this error is minimized if the sample has a cylidrical symmetry. Although not realistic in a biological sense, the use of cylindrical phantoms, which has been used widely by others (Zhang *et al* 2013a, Lee *et al* 2015c), provides an accessible means of testing the homogeneous Helmholtz EPT calculations. For the current cylindrical phantoms with diameters less than 3 cm at 21.1 T, the relative agreement of results with dielectric probe measurements demonstrate the potential and limitations of implementing Helmholtz-based EPT with the transceive phase assumption, as error analysis displays the higher susceptibility of conductivity estimates to all sources of phase error in comparison to permittivity estimates. In fact, permittivity measurements displayed good agreement with the dielectric probe and improved accuracy compared to lower fields. Promising results also have been collected for EP measurement of *ex* and *in vivo* rat brains using the same method, but point to the limitations of the approach and need for more elegant approaches to preserve resolution and reduce variability.

For the linear birdcage and even with violation of the transceive phase assumption at 900 MHz, an average percent difference of 23% for the Full-form EPT as compared to the dielectric probe measurement across all salinities was calculated (Table 1), with the lowest error of 11% evident in the highest conductivity. This average error is in line with the previous Full-form EPT studies at lower fields (Katscher *et al* 2009), which showed a mean error range from 3-20%. The Phase-based approach yielded on average a 49% difference from the conductivity values, which is at the lower end of the 44-100% reported at 7 T (van Lier *et al* 2012a). Table 2 also shows higher percent error and RMSE for the Phase-based approach versus the Full-form for the linear birdcage coil, reinforcing that there is a penalty for ignoring the gradient of B_1^+ field even with the relatively uniform B_1^+ profile excited by the birdcage. This penalty differentially impacts the samples evaluated but tends to be greater for samples (tubes 2 and 3) placed near the feed points of the birdcage or samples (tube 1) that have lower conductivities and may be susceptible to dielectric resonance effects. Based on this evaluation, EPT conducted at 21.1 T appears to introduce an average error of 0.47 S/m for the full-form approach; the exclusion of the B_1 magnitude term used in the Phase-only approach increases this error by a factor of 40%.

Outside of phased arrays, few previous studies have investigated implementing EPT with a surface transceive coil configuration, which motivated the evaluation of the quadrature saddle coil at 21.1 T (900 MHz). Based on the standard deviations, increased SNR of the quadrature saddle coil display tangible benefits in improving at least the variability and precision of the EPT estimates. However, as displayed in Figure 4, RF inhomogeneities resulting from B_1 drop-off from the surface of the saddle coil and the generation of standing waves from propagation in a quasi-uniform medium at low conductivities do impact the measured estimates of conductivity. Using the conductivity and relative permittivity of tube 1, the skin depth is δ_1 = 23.6 cm (Bottomley and

Andrew 1978) while the wavelength of the B_1 field is $\lambda_1 = 3.67$ cm. With a sample diameter of 1.4 cm ($>\lambda_1/4$), length of 4 cm ($>\lambda_1$) and with no effective attenuation provided by the skin depth, tube 1 experiences standing wave formation similar to dielectric resonance in at least the z-direction. As a result, considerable phase shift and inhomogeneity in the B_1 field unrelated to the conductivity are expected and evident in tube 1, affecting the error percentages for both conductivity reconstruction approaches, though more heavily the Full-form due to its inclusion of the B_1^+ magnitude term. For tube 4 with significant conductivity that yields skin depth of $\delta_4 = 1.26$ cm, the lossy sample attenuates wave propagation and does not permit standing waves to develop. As a result, higher conductivity dominates the B_1^+ phase and magnitude profile, resulting in increased accuracy for conductivity reconstructions.

As shown in Tables 1 and 2 for the saddle coil, the Full-form conductivity has an average difference of 86% from the dielectric probe across all salinities while the Phase-based approach yields an average 63% difference, though both averages are weighted heavily by the lowest conductivity that it is impacted by dielectric resonance effects. In comparison to the birdcage coil, the RMSE are more informative, as Full-form EPT of the quadrature coil shows an average of 0.68 S/m, which is 46% higher than the average Full-form RMSE for the birdcage, while Phase-based EPT shows the lowest RMSE of all approaches at an average of 0.44 S/m.

In addition to conductivity, the possibility of reconstructing permittivity was investigated in the phantom. Reconstructed permittivity values are in excellent agreement with the dielectric probe and show an average difference error of 7% and 5% in the Full-form and Magnitude-based reconstructions, respectively, indicating major improvements in the EPT estimations resulting from increased field strength. Permittivity measurements conducted on phantoms at 1.5 T displayed on average 26-90% error from the target; however, studies at 3 and 7 T showed 2-44%

and 3-4% errors, respectively (van Lier *et al* 2012a). A recent study on the impact of B_1 mapping techniques for permittivity reconstructions reported a percent error of 4-54% in phantoms at 3 T depending on the B_1 mapping approach, although standard deviations were found to be greater than 50% of the reported mean permittivity regardless (Gavazzi *et al* 2019).

Reinforcing the improvement at 21.1 T, the RMSE of measured relative permittivities are consistent across all samples and between the two techniques. Admittedly, the current phantom does not provide a wide range of permittivities; however, it is notable that the lowest permittivity of tube 4 was determined to be significantly different from the other tubes for both reconstructions. This finding underscores the sensitivity of high field EPT to detect even small permittivity changes, even at the level of a 7-10% change in ε_r, with the Magnitude-based as robust as the Full-form reconstruction. Reduced error percentages and RMSE for the measurement of relative permittivity compared to conductivity indicate the relative robustness of permittivity reconstructions with respect to the violation of transceive phase assumption for 21.1 T.

In both conductivity and permittivity reconstructions of the phantom, the violation of the homogeneity assumption in the Helmholtz equations at the sample boundaries and the numerical calculation of the Laplacian have resulted in so-called "boundary artifacts." At these boundaries, the application of the Laplacian kernel over regions with drastically different EP induces discontinuity that corrupts the EP measurement over a number of interfacial pixels, which are proportional to the width of the Laplacian kernel. As a result, although they offer noise robustness, larger kernel sizes still produce larger boundary artifacts. This limitation is consistent with most EPT approaches that utilize a numerical Laplacian, and high field has no impact on these artifacts but the reduced preclinical sample size (either of phantoms or animal neuroanatomy) does magnify the impact of such artifacts. For phantom experiments, the central regions of each sample tube provided at least an area of 4000 pixel^2, which was sufficient for EP estimations. However, the limitations of the homogenous Helmholtz EPT approach in this regard constrains the sample regions that can be analyzed while reducing the overall resolution of the EP maps. Additionally, variability in EPT data and relatively high standard deviations result from the implementation of the numerical Laplacian intrinsic to Helmoltz-based EPT. Effecting the conductivity calculation more than the permittivity, the derivative of the B_1^+ phase (either 2nd or 1st order) is impacted by any phase noise. Other EPT reconstruction approaches that better accommodate transitions between boundaries and decrease or eliminate reliance on the numerical Laplacian (Jin Keun Seo *et al* 2012, Liu *et al* 2018, Borsic *et al* 2016, Guo *et al* 2018) may prove much more applicable at very high field. However, these alternatives often utilize multi-transmit phased array capabilities (Liu *et al* 2015, Zhang *et al* 2013a, Liu *et al* 2017a), which may not be available on preclinical systems (such as the current 21.1-T system employed here), but may motivate instrumentation enhancements to make more complete use of EPT approaches at high field.

In addition to the phantom study, the feasibility of reconstructing EP of the rat brain also was investigated using Helmholtz-based EPT at 21.1 T. For both *ex* and *in vivo* cases, the Phase-based conductivity and Magnitude-based permittivity reconstructions were compared with the Full-form calculations. The conductivity and permittivity results do not show a difference between the two forms of reconstructions for biological tissue. As such, the simplified techniques of Phase-based conductivity and Magnitude-based permittivity mapping appear to be as robust as the Full-form at 21.1 T for biological application. Due to the large noise-robust kernels employed in the Laplacian calculation, boundary artifacts are evident at the brain periphery, and there may be tissue boundary artifacts that are present within the more central brain. With non-homogeneous EP compartments, this limitation of Hemholtz-based EPT is significant for the reduced dimensions of preclinical neuroanatomy, and does not permit for the full resolution or sensitivity of high field EPT to be utilized.

Based on the ROI analysis, the mean conductivities and permittivities calculated for rodents at 21.1 T are in good agreement with theoretical EP values based on the Cole-Cole model for excised gray matter of the human brain at 900 MHz, which predicts $\sigma = 0.94$ S/m and $\varepsilon_r = 52.72$ (Gabriel 1996). Using Phase-based and Magnitude-based calculations, the percent difference between these theoretical values and the *ex vivo* EPT conductivity and permittivity are 3% and 9%, respectively. For measures in the non-pathological regions of the *in vivo* rat brain, the percent differences from the Cole-Cole model are higher, with the conductivity 31% higher and the *in vivo* permittivity 26% lower. It should be noted that the Cole-Cole model is specific for excised human gray matter, and thus is not impacted by blood flow, motion, temperature and volume averaging across different tissue types (*i.e.*, gray matter, white matter and CSF) and neuroanatomical structures as in the *in vivo* rat experiments conducted at 21.1 T. Human studies of *in vivo* brain conductivity at 7 T using Helmholtz-based EPT also yielded higher conductivities than predicted by the Cole-Cole model, namely average EPT conductivity was 26% and 63% higher for gray and white matter, respectively (van Lier *et al* 2012a). *In vivo* permittivity assessments in human brain and abdomen up to 7 T did not yield robust permittivity Helmholtz-based EPT estimates that could be deemed reliable or quantitative, limiting their utility in clinically acceptable scans (Gavazzi *et al* 2019, Van Lier *et al* 2014). In a preliminary study conducted in a limited *ex vivo* rat cohort (Jensen-Kondering *et al* 2017), brain conductivities at 3 T for gray and white matter were 42% and 84% higher, respectively, than the Cole-Cole prediction for 128 MHz. Also, in a study of RF exposure over cellular communication frequencies (Peyman *et al* 2001), the average dielectric probe measured conductivity and relative permittivity ranges at 881 MHz for intact brains excised

2-4 h after sacrifice were 0.8-0.7 S/m (<1.08% standard deviation) and 49.2-44.3 (<6.15% standard deviation), respectively, for 30-50 day-old Wistar rats, which is in good agreement with the current *ex* and *in vivo* EPT measures at 900 MHz. Therefore, *in vivo* overestimation of conductivity at 21.1 T is at least consistent if not better than published values, with permittivity measures displaying even higher degrees of consistency, which supports the potential of EPT at 21.1 T to provide reliable quantitative estimates in accessible scan times.

More critically, the EPT values evident in the subacute ischemic lesion demonstrate a large increase in Phase-based conductivity (48%) and Magnitude-based permittivity (55%) compared to the contralateral side and more distal non-pathological regions of the *in vivo* rat brain. As such, these measures indicate significant remodeling of ischemic tissue with a high degree of detectability using Helmholtz-based EPT. Supporting this finding, previous single-patient case studies of ischemic stroke have reported elevated conductivity although with some exceptions (van Lier *et al* 2012b, Gurler *et al* 2016). In preclinical evaluations at 3 T, the work of Kim et al. identified a 43.2% increase in conductivity of canine brain 12 h after cerebral ischemia using Helmholtz-based EPT (Kim *et al* 2015), which is in excellent agreement with the current study's findings. In another preliminary study conducted at 3 T, an *in vivo* transient MCAO rat also demonstrated conductivity increases on the order of 2.5 times the contralateral side (Jensen-Kondering *et al* 2017).

Uniquely, the current study demonstrates a large increase in permittivity for *in vivo* subacute stroke. This effect has not been evaluated thoroughly in the literature. However, one *ex vivo* study of edematous tissue (Kao *et al* 1999) conducted on canine white matter did display a positive correlation between increased water content and higher permittivity over 100-1000 MHz. Although not examining ischemic tissue specifically, the aforementioned RF study (Peyman *et al*

2001) demonstrated consistently decreasing conductivity (>16%) and permittivity (>10%) as measured by dielectric probe for intact excised rat brain from 0-70 days, which was attributed primarily to the loss of water content and decrease in free-to-bound water fraction with age and structural maturation. Likewise, the recent work of Michel et al. (Michel *et al* 2017) correlated the anatomically specific water content to conductivity and permittivity, showing that increased EP were evident for structures and tissue types with higher percentages of water. As EP in biological tissue reflect water and ionic content at high frequency (Oh *et al* 2011, Schwan and Foster 1989), the alteration detected in the EP of the ischemic lesion can be explained by tissue compartment changes following the disruption of cerebral blood flow, which result in the presence of edema as well as increases in sodium concentrations extra- and intracellularly during the subacute phase (Lee *et al* 2015a, Roussel *et al* 2018, Hussain *et al* 2009, Tsang *et al* 2011, Moseley *et al* 1990, Boada *et al* 2005). As such, the increased EP values 24 h post MCAO are consistent with the established increase in tissue water content (displayed by ^{1}H FSE in Fig 6a) and sodium (evidenced by ^{23}Na GRE in Fig 6d). The observed increase in the EP of ischemic stroke lesion indicates the importance of further studies and more applicable EPT approaches to track stroke and its dynamic evolution.

Conclusions

In this study, conductivity and permittivity mapping were implemented using Helmholtz-based EPT for ultra-high field (21.1 T). Based on previous studies at fields higher than 3 T, wave interference patterns affecting B_1^+ phase and magnitude can introduce error in the EPT reconstruction, decreasing the validity of Phase-based approach (Van Lier *et al* 2014). However, electrical properties and sample/coil geometry also should be considered. For operation at 900 MHz, sample sizes of less than the RF wavelength and increased sample conductivity were shown to minimize the wave interferences such that the calculated conductivity values are in relative agreement with the target using either the Full-form or Phase-based approach. The estimated conductivity values from these two approaches verified that only considering second order variation of transceive phase still approximates the target conductivity, although incorporation of the $|B_1^+|$ does improve measurement accuracy and precision if the RF field characteristics (such as dielectric resonance or B_1^+ drop-off as seen in the saddle coil experiments) do not dominate and confound the EPT estimations. Overall, the study shows that the error between Phase-based and Full-form approaches is approximately 25% of the target value at this field strength.

Permittivity mapping at 21.1 T showed a significant improvement in comparison to lower fields. Relative permittivity measured in each tube of the phantom was in good agreement with the dielectric probe value. Additionally, the error between the Full-form or Magnitude-based approach in calculating relative permittivity was less than 5% of the target value, indicating that permittivity distribution is mostly defined by B_1 curvature at higher field.

The feasibility of EP mapping for *in vivo*, as well as *ex vivo* rat brains, were investigated in a limited cohort of specimens. Although Helmholtz-based EPT in rat brain significantly suffers from tissue boundaries artifacts and variability, reasonable conductivity and permittivity values were derived from selected ROI. However, limited resolution and contrast were provided solely by homogenous Helmholtz-based EPT. Encouragingly, as a proof of principle, *in vivo* results showed elevated conductivity and permittivity for an ischemic lesion, reflecting the increased water content and sodium elevation in this region and potentially indicating that permittivity measures may be more robust to ischemia-related alterations. With application of EPT reconstruction approaches that better address heterogeneous compartments over preclinical length scales, conductivity and permittivity as a function of time post occlusion may be able to map the evolution of ischemia over acute and chronic phases.

Although the current findings demonstrate the limited utility of Helmholtz-based EPT approaches at high magnetic fields, these numerical approaches offer the potential for increased precision and reduced error at high field (particularly for permittivity measures). The evident limitations to resolution and variability also serve as motivation for more advanced EPT reconstruction to be pursued, particularly those that avoid the transceive phase assumption (Hafalir *et al* 2014, Liu *et al* 2015, Gurler and Ider 2016, Liu *et al* 2018). As such, this study has ramifications for electrical property tomography at ultra-high field for both materials and biological applications.

Compliance with ethical standards

Conflict of interest

The authors declare that they have no conflict of interest.

Ethical approval

All procedures performed in studies were in accordance with the ethical standards of the institutional and/or national research committee and with the 1964 Helsinki Declaration and its later amendments or comparable ethical standards.

References

Alecci M, Collins C M, Smith M B and Jezzard P 2001 Radio frequency magnetic field mapping of a 3 Tesla birdcage coil: Experimental and theoretical dependence on sample properties *Magn. Reson. Med.* **46** 379–85

Ammari H, Kwon H, Lee Y, Kang K and Seo J K 2015 Magnetic resonance-based reconstruction method of conductivity and permittivity distributions at the Larmor frequency *Inverse Probl.* **31** 105001

Amouzandeh G, Rosenberg J T, Mentink-vigier F, Abad N and Grant S C 2018 Evaluating Validity of MREPT Assumptions for 21.1 T *Proc. Intl. Soc. Mag. Reson. Med. 26th* (Paris, France) p 5088

Arduino A, Bottauscio O, Chiampi M and Zilberti L 2018 Magnetic resonance-based imaging of human electric properties with phaseless contrast source inversion *Inverse Probl.* **34** 084002

Balidemaj E, de Boer P, van Lier A L H M W, Remis R F, Stalpers L J A, Westerveld G H, Nederveen A J, van den Berg C A T and Crezee J 2016 In vivo electric conductivity of cervical cancer patients based on B1+ maps at 3T MRI *Phys. Med. Biol.* **61** 1596–607

Balidemaj E, van Lier A L H M W, Crezee H, Nederveen A J, Stalpers L J A and van den Berg C A T 2015 Feasibility of Electric Property Tomography of pelvic tumors at 3T *Magn. Reson. Med.* **73** 1505–13

Bernstein M A, King K F and Zhou X J 2004 Chapter 10 *Handbook of MRI pulse sequences* (Elsevier Inc.) pp 316–30

Bevacqua M T, Bellizzi G G, Crocco L and Isernia T 2019 A method for quantitative imaging of electrical properties of human tissues from only amplitude electromagnetic data *Inverse Probl.* **35** 025006

Boada F E, LaVerde G, Jungreis C, Nemoto E, Tanase C and Hancu I 2005 Loss of cell ion homeostasis and cell viability in the brain: What sodium MRI can tell us *Current topics in developmental biology* vol 70 pp 77–101

Borsic A, Perreard I, Mahara A and Halter R J 2016 An Inverse Problems Approach to MR-EPT Image Reconstruction *IEEE Trans. Med. Imaging* **35** 244–56

Bottomley P A and Andrew E R 1978 Rf Magnetic-Field Penetration, Phase-Shift and Power Dissipation in Biological Tissue - Implications for Nmr Imaging *Phys. Med. Biol.* **23** 630–43

Bulumulla S B, Lee S K and Yeo D T B 2012 Conductivity and permittivity imaging at 3.0 T *Concepts Magn. Reson. Part B Magn. Reson. Eng.* **41B** 13–21

Collins C M, Liu W, Schreiber W, Yang Q X and Smith M B 2005 Central brightening due to constructive interference with, without, and despite dielectric resonance *J. Magn. Reson. Imaging* **21** 192–6

Collins C M, Liu W, Wang J, Gruetter R, Vaughan J T, Ugurbil K and Smith M B 2004 Temperature and SAR calculations for a human head within volume and surface coils at 64 and 300 MHz *J. Magn. Reson. Imaging* **19** 650–6

Cunningham C H, Pauly J M and Nayak K S 2006 Saturated double-angle method for rapid B1+ mapping *Magn. Reson. Med.* **55** 1326–33

Duan S, Xu C, Deng G, Wang J, Liu F and Xin S X 2016 Quantitative analysis of the reconstruction errors of the currently popular algorithm of magnetic resonance electrical property tomography at the interfaces of adjacent tissues *NMR Biomed.* **29** 744–50

Fu R, Brey W W, Shetty K, Gor'kov P, Saha S, Long J R, Grant S C, Chekmenev E Y, Hu J, Gan Z, Sharma M, Zhang F, Logan T M, Brüschweller R, Edison A, Blue A, Dixon I R, Markiewicz W D and Cross T A 2005 Ultra-wide bore 900 MHz high-resolution NMR at the National High Magnetic Field Laboratory *J. Magn. Reson.* **177** 1–8

Gabriel C 1996 Compilation of the Dielectric Properties of Body Tissues at RF and Microwave Frequencies *U.S. Air Force Rep. AFOSR-TR-96*

Gabriel S, Lau R W, Gabriel C, Bateman J B G C and G E H, Foster K R S J L S R D and S H P, P F K R and S H, Gabriel C G S and C E, Gabriel C S R J and G E H, Gabriel S L R W and G C, Grant E H S R J and S G P, D H W and R S J L and F K 1996 The dielectric properties of biological tissues: III. Parametric models for the dielectric spectrum of tissues *Phys. Med. Biol.* **41** 2271–93

Gavazzi S, Berg C A T, Sbrizzi A, Kok H P, Stalpers L J A, Lagendijk J J W, Crezee H and Lier A L H M W 2019 Accuracy and precision of electrical permittivity mapping at 3T: the impact of three mapping techniques *Magn. Reson. Med.* **81** 3628–3642

Goldstein R M, Zebker H A and Werner C L 1988 Satellite radar interferometry: Two-dimensional phase unwrapping *Radio Sci.* **23** 713–20

Guo L, Jin J, Li M, Wang Y, Liu C yi, Liu F and Crozier S 2018 Reference-Based Integral MR-EPT:Simulation and Experiment Studies on the 9.4T MRI *IEEE Trans. Biomed. Eng.* 1–1

Gurler N and Ider Y Z 2016 Gradient-based electrical conductivity imaging using MR phase *Magn. Reson. Med.* **77** 137–50

Gurler N, Oran O, Keklikoglu H and Ider Y 2016 Application of Generalized Phase based Electrical Conductivity Imaging in the Subacute Stage of Hemorrhagic and Ischemic Strokes *Proc. Intl. Soc. Mag. Reson. Med. 24th* (Singapore) p 2994

Haacke E M, Petropoulos L S, Nilges E W and Wu D H 1991 Extraction of conductivity and permittivity using magnetic resonance imaging *Phys. Med. Biol.* **36** 723–34

Hafalir F S, Oran O F, Gurler N and Ider Y Z 2014 Convection-Reaction Equation Based Magnetic Resonance Electrical Properties Tomography (cr-MREPT) *IEEE Trans. Med. Imaging* **33** 777–93

Hancu I, Roberts J C, Bulumulla S and Lee S-K 2015 On conductivity, permittivity, apparent diffusion coefficient, and their usefulness as cancer markers at MRI frequencies *Magn. Reson. Med.* **73** 2025–9

Holoborodko P 2009 Noise Robust Gradient Operators http://www.holoborodko.com/pavel/image-processing/edge-detection/2009

Huhndorf M, Stehning C, Rohr A, Helle M, Katscher U and Jansen O 2013 Systematic Brain Tumor Conductivity Study with Optimized EPT Sequence and Reconstruction Algorithm *Proc. Intl. Soc. Mag. Reson. Med. 21st* (Salt Lake City, Utah, USA) p 3626

Hussain M S, Stobbe R W, Bhagat Y A, Emery D, Butcher K S, Manawadu D, Rizvi N, Maheshwari P, Scozzafava J, Shuaib A and Beaulieu C 2009 Sodium imaging intensity increases with time after human ischemic stroke *Ann. Neurol.* **66** 55–62

Jensen-Kondering U, Böhm R, Shu L, Jansen O and Katscher U 2017 Electric properties tomography in a rodent model of ischemic stroke: Results of a combined ex-vivo and in-vivo pilot study *Proc. Intl. Soc. Mag. Reson. Med. 25th* (Honolulu, HI, USA) p 4627

Jin Keun Seo, Min-Oh Kim, Joonsung Lee, Narae Choi, Eung Je Woo, Hyung Joong Kim, Oh In Kwon and Dong-Hyun Kim 2012 Error Analysis of Nonconstant Admittivity for MR-Based Electric Property Imaging *IEEE Trans. Med. Imaging* **31** 430–7

Joines W T, Zhang Y, Li C and Jirtle R L 1994 The measured electrical properties of normal and malignant human tissues from 50 to 900 MHz *Med. Phys.* **21** 547–50

Kaatze U 1997 The Dielectric Properties of Water in Its Different States of Interaction *J. Solution Chem.* **26**

Kao H P, Cardoso R and Shwedyk E 1999 Correlation of permittivity and water content during cerebral edema *IEEE Trans. Biomed. Eng.* **46** 1121–8

Katscher U and van den Berg C A T 2017 Electric properties tomography: Biochemical, physical and technical background, evaluation and clinical applications *NMR Biomed.* **30** e3729

Katscher U, Hiroyuki A, Ivancevic M K, Djamshidi K, Karkowski P and Newstead G 2013a Towards the investigation of breast tumor malignancy via electric conductivity measurement *Proc. Intl. Soc. Mag. Reson. Med. 21st* (Salt Lake City, Utah, USA) p 3372

Katscher U, Kim D and Seo J K 2013b Recent Progress and Future Challenges in MR Electric Properties Tomography *Comput. Math. Methods Med.* **2013** 1–11

Katscher U, Voigt T, Findeklee C, Vernickel P, Nehrke K and Dossel O 2009 Determination of Electric Conductivity and Local SAR Via B1 Mapping *IEEE Trans. Med. Imaging* **28** 1365–74

Kim D H, Chauhan M, Kim M O, Jeong W C, Kim H J, Sersa I, Kwon O I and Woo E J 2015 Frequency-dependent conductivity contrast for tissue characterization using a dual-frequency range conductivity mapping magnetic resonance method *IEEE Trans. Med. Imaging* **34** 507–13

Kim S Y, Shin J, Kim D H, Kim E K, Moon H J, Yoon J H, You J K and Kim M J 2018 Correlation between electrical conductivity and apparent diffusion coefficient in breast cancer: effect of necrosis on magnetic resonance imaging *Eur. Radiol.* **28** 3204–14

Kim S Y, Shin J, Kim D H, Kim M J, Kim E K, Moon H J and Yoon J H 2016 Correlation between conductivity and prognostic factors in invasive breast cancer using magnetic resonance electric properties tomography (MREPT) *Eur. Radiol.* **26** 2317–26

Kwon O, Jeong W, K Sajib S Z, Kim H, Woo E and Oh T 2014 Reconstruction of dual-frequency conductivity by optimization of phase map in MREIT and MREPT *Biomed. Eng. Online* **13** 24

Lazebnik M, Popovic D, McCartney L, Watkins C B, Lindstrom M J, Harter J, Sewall S, Ogilvie T, Magliocco A, Breslin T M, Temple W, Mew D, Booske J H, Okoniewski M and Hagness S C 2007 A large-scale study of the ultrawideband microwave dielectric properties of normal, benign and malignant breast tissues obtained from cancer surgeries *Phys. Med. Biol.*

Lee K-C, Yu J-F, Lee Y-S, Huang G-J, Chan H-L, Lin I-T and Chen J-H 2015a In Vivo Sodium MRI for Mouse Model of Ischemic Stroke at 7 T: Preliminary Results *J. Med. Biol. Eng.* **35** 643–50

Lee S K, Bulumulla S and Hancu I 2015b Theoretical Investigation of Random Noise-Limited Signal-to-Noise Ratio in MR-Based Electrical Properties Tomography *IEEE Trans. Med. Imaging* **34** 2220–32

Lee S K, Bulumulla S, Wiesinger F, Sacolick L, Sun W and Hancu I 2015c Tissue electrical property mapping from zero echo-time magnetic resonance imaging *IEEE Trans. Med. Imaging* **34** 541–50

Leijsen R, Fuchs P, Brink W, Webb A, Remis R, Leijsen R, Fuchs P, Brink W, Webb A and Remis R 2019 Developments in Electrical-Property Tomography Based on the Contrast-Source Inversion Method *J. Imaging* **5** 25

Li C, Yu W and Huang S Y 2017 An MR-Based Viscosity-Type Regularization Method for Electrical Property Tomography *Tomography* **3** 50–9

van Lier A L H M W, Brunner D O, Pruessmann K P, Klomp D W J, Luijten P R, Lagendijk J J W and van den Berg C A T 2012a B 1+ Phase mapping at 7 T and its application for in vivo electrical conductivity mapping *Magn. Reson. Med.* **67** 552–61

van Lier A L H M W, van der Kolk A G, Brundel M, Hendrikse J, Luijten P R, Lagendijk J J W and van den Berg C A T 2012b Electrical conductivity in ischemic stroke at 7.0 Tesla: A Case Study *Proc. Intl. Soc. Mag. Reson. Med. 20* (Melbourne, Australia) p 3484

Van Lier A L H M W, Raaijmakers A, Voigt T, Lagendijk J J W, Luijten P R, Katscher U and

Van Der Berg C A T 2014 Electrical properties tomography in the human brain at 1.5, 3, and 7T: A comparison study *Magn. Reson. Med.* **71** 354–63

Van Lier A L, Hoogduin J M, Polders D L, Boer V O, Hendrikse J, Robe P A, Woerdeman P A, Lagendijk J J, Luijten P R and Van Den Berg C A 2011 Electrical conductivity imaging of brain tumours *Proc. Intl. Soc. Mag. Reson. Med. 19th* (Montréal, Québec, Canada) p 4464

Liu C, Jin J, Guo L, Li M, Tesiram Y, Chen H, Liu F, Xin X and Crozier S 2018 MR-based electrical property tomography using a modified finite difference scheme *Phys. Med. Biol.* **63** 145013

Liu J, Shao Q, Wang Y, Adriany G, Bischof J, Van de Moortele P-F and He B 2017a In vivo imaging of electrical properties of an animal tumor model with an 8-channel transceiver array at 7 T using electrical properties tomography *Magn. Reson. Med.* **78** 2157–69

Liu J, Wang Y, Katscher U and He B 2017b Electrical Properties Tomography Based on B1 Maps in MRI: Principles, Applications, and Challenges *IEEE Trans. Biomed. Eng.* **64** 2515–30

Liu J, Zhang X, Van de Moortele P-F, Schmitter S and He B 2013 Determining electrical properties based on B 1 fields measured in an MR scanner using a multi-channel transmit/receive coil: a general approach *Phys. Med. Biol.* **58** 4395–408

Liu J, Zhang X, Schmitter S, Van de Moortele P-F and He B 2015 Gradient-based electrical properties tomography (gEPT): A robust method for mapping electrical properties of biological tissues in vivo using magnetic resonance imaging *Magn. Reson. Med.* **74** 634–46

Longa E Z, Weinstein P R, Carlson S and Cummins R 1989 Reversible middle cerebral artery occlusion without craniectomy in rats. *Stroke* **20** 84–91

Mandija S, Sbrizzi A, Katscher U, Luijten P R and van den Berg C A T 2017 Error analysis of helmholtz-based MR-electrical properties tomography *Magn. Reson. Med.*

Michel E, Hernandez D, Cho M H and Lee S Y 2014 Denoising of B1+ field maps for noise-robust image reconstruction in electrical properties tomography *Med. Phys.* **41** 102304

Michel E, Hernandez D and Lee S Y 2017 Electrical conductivity and permittivity maps of brain tissues derived from water content based on T1-weighted acquisition *Magn. Reson. Med.* **77** 1094–103

Moseley M E, Cohen Y, Mintorovitch J, Chileuitt L, Shimizu H, Kucharczyk J, Wendland M F and Weinstein P R 1990 Early detection of regional cerebral ischemia in cats: Comparison of diffusion- and T2-weighted MRI and spectroscopy *Magn. Reson. Med.* **14** 330–46

Motovilova E, Su J and Huang S Y 2015 MRI-based electrical property mapping for human body *2015 IEEE International Conference on Computational Electromagnetics* (IEEE) pp 73–5

Muniz J A, Elumalai M, Masad I S, Brey W W, Gor ’kov P . and Grant S C 2011 Quadrature RF Coil and Phased Array Operation at 21.1 T *Proceedings of the 19th Annual Meeting of ISMRM* p 1825

Oh T I, Kim Y T, Minhas A, Seo J K, Kwon O I and Woo E J 2011 Ion mobility imaging and contrast mechanism of apparent conductivity in MREIT *Phys. Med. Biol.* **56** 2265–77

Ouwerkerk R, Jacobs M A, MacUra K J, Wolff A C, Stearns V, Mezban S D, Khouri N F, Bluemke D A and Bottomley P A 2007 Elevated tissue sodium concentration in malignant breast lesions detected with non-invasive 23Na MRI *Breast Cancer Res. Treat.*

Overall W R, Pauly J M, Stang P P and Scott G C 2010 Ensuring safety of implanted devices under MRI using reversed RF polarization. *Magn. Reson. Med.* **64** 823–33

Pethig R 1984 Dielectric Properties of Biological Materials: Biophysical and Medical Applications *IEEE Trans. Electr. Insul.* **EI-19** 453–74

Peyman A, Rezazadeh A A and Gabriel C 2001 Changes in the dielectric properties of rat tissue as a function of age at microwave frequencies *Phys. Med. Biol.* **46** 1617–29

Qian C, Masad I S, Rosenberg J T, Elumalai M, Brey W W, Grant S C and Gor’kov P L 2012 A volume birdcage coil with an adjustable sliding tuner ring for neuroimaging in high field vertical magnets: ex and in vivo applications at 21.1T. *J. Magn. Reson.* **221** 110–6

Rosenberg J T, Shemesh N, Muniz J A, Dumez J-N, Frydman L and Grant S C 2017 Transverse relaxation of selectively excited metabolites in stroke at 21.1 T *Magn. Reson. Med.* **77** 520–8

Roussel T, Rosenberg J T, Grant S C and Frydman L 2018 Brain investigations of rodent disease models by chemical exchange saturation transfer at 21.1 T *NMR Biomed.* **31** e3995

Schepps J L and Foster K R 1980 The UHF and microwave dielectric properties of normal and tumour tissues: variation in dielectric properties with tissue water content *Phys. Med. Biol* **25** 1149–59

Schwan H P and Foster K R 1989 Dielectric properties of tissues and biological materials: a ceritical review *Crit. Rev. Biomed. Eng.* **17** 25–104

Seo J K, Woo E J, Katscher U and Wang Y 2014 *Electro-Magnetic Tissue Properties MRI* vol 1 (IMPERIAL COLLEGE PRESS)

Serralles J E C, Daniel L, White J K, Sodickson D K, Lattanzi R and Polimeridis A G 2016 Global maxwell tomography: A novel technique for electrical properties mapping based on MR measurements and volume integral equation formulations *2016 IEEE International Symposium on Antennas and Propagation (APSURSI)* (IEEE) pp 1395–6

Shin J, Kim J-H and Kim D-H 2019 Redesign of the Laplacian kernel for improvements in conductivity imaging using MRI *Magn. Reson. Med.* **81** 2167–75

Shin J, Kim M J, Lee J, Nam Y, Kim M, Choi N, Kim S and Kim D-H 2015 Initial study on in vivo conductivity mapping of breast cancer using MRI *J. Magn. Reson. Imaging* **42** 371–8

Stollberger R and Wach P 1997 Erratum: Imaging of the active B1 field in vivo (Magnetic Resonance in Medicine (1996) 35 (246-251)) *Magn. Reson. Med.* **38** 336

Tha K K, Katscher U, Yamaguchi S, Stehning C, Terasaka S, Fujima N, Kudo K, Kazumata K, Yamamoto T, Van Cauteren M and Shirato H 2018 Noninvasive electrical conductivity measurement by MRI: a test of its validity and the electrical conductivity characteristics of glioma *Eur. Radiol.* **28** 348–55

Tsang A, Stobbe R W, Asdaghi N, Hussain M S, Bhagat Y A, Beaulieu C, Emery D and Butcher K S 2011 Relationship between sodium intensity and perfusion deficits in acute ischemic stroke *J. Magn. Reson. Imaging* **33** 41–7

Vaidya M V, Collins C M, Sodickson D K, Brown R, Wiggins G C and Lattanzi R 2016 Dependence of B1+ and B1- Field Patterns of Surface Coils on the Electrical Properties of the Sample and the MR Operating Frequency. *Concepts Magn. Reson. Part B. Magn. Reson. Eng.* **46** 25–40

Voigt T, Homann H, Katscher U and Doessel O 2012 Patient-individual local SAR determination: In vivo measurements and numerical validation *Magn. Reson. Med.* **68**

1117–26

Voigt T, Katscher U and Doessel O 2011 Quantitative conductivity and permittivity imaging of the human brain using electric properties tomography *Magn. Reson. Med.* **66** 456–66

Wang Y, Van De Moortele P-F and He B 2019a CONtrast Conformed Electrical Properties Tomography (CONCEPT) Based on Multi- Channel Transmission and Alternating Direction Method of Multipliers *IEEE Trans. Med. Imaging* **38** 349–59

Wang Y, Shao Q, Van de Moortele P-F, Racila E, Liu J, Bischof J and He B 2019b Mapping electrical properties heterogeneity of tumor using boundary informed electrical properties tomography (BIEPT) at 7T *Magn. Reson. Med.* **81** 393–409

Webb A G and Grant S C 1996 Signal-to-noise and magnetic susceptibility trade-offs in solenoidal microcoils for NMR. *J. Magn. Reson. B* **113** 83–7

Wen H 2003 Noninvasive quantitative mapping of conductivity and dielectric distributions using RF wave propagation effects in high-field MRI *Proc. SPIE 5030, Medical Imaging: Physics of Medical Imaging* vol 5030, ed M J Yaffe and L E Antonuk p 471

Xiaotong Zhang, Jiaen Liu and Bin He 2014 Magnetic-Resonance-Based Electrical Properties Tomography: A Review *IEEE Rev. Biomed. Eng.* **7** 87–96

Xiaotong Zhang, Shanan Zhu and Bin He 2010 Imaging Electric Properties of Biological Tissues by RF Field Mapping in MRI *IEEE Trans. Med. Imaging* **29** 474–81

Yang Q X, Wang J, Zhang X, Collins C M, Smith M B, Liu H, Zhu X-H, Vaughan J T, Ugurbil K and Chen W 2002 Analysis of wave behavior in lossy dielectric samples at high field *Magn. Reson. Med.* **47** 982–9

Zhang X, Van de Moortele P-F, Liu J, Schmitter S and He B 2014 Quantitative prediction of radio frequency induced local heating derived from measured magnetic field maps in magnetic resonance imaging: A phantom validation at 7 T *Appl. Phys. Lett.* **105** 244101

Zhang X, de Moortele P-F Van, Schmitter S and He B 2013a Complex B1 mapping and electrical properties imaging of the human brain using a 16-channel transceiver coil at 7T *Magn. Reson. Med.* **69** 1285–96

Zhang X, Schmitter S, Van de Moortele P-F, Liu J and He B 2013b From complex B1 mapping to Local SAR estimation for human brain MR imaging using multi-channel transceiver coil at 7T *IEEE Trans. Med. Imaging* **32** 1058–67